AIAA 99-0241

Effect of Inlet Conditions on Endwall Secondary Flows

Kristina S. Hermanson
Karen A. Thole
Mechanical Engineering Department
University of Wisconsin-Madison
Madison, WI

37th AIAA Aerospace Sciences Meeting and Exhibit
January 11-14, 1999 / Reno, NV

AIAA-99-0241

EFFECT OF INLET CONDITIONS ON ENDWALL SECONDARY FLOWS

Kristina S. Hermanson and Karen A. Thole
Mechanical Engineering Department
University of Wisconsin
Madison, Wisconsin 53706

Abstract

Exit combustor flow and thermal fields entering downstream stator vane passages in a gas turbine engine are highly non-uniform. These flow and thermal fields can significantly affect the development of the secondary flows in the turbine passages attributing to high platform heat transfer and large aerodynamic losses. This paper presents an analysis of the effects of both the temperature and velocity profiles on the secondary flows in the endwall region of a first stage stator vane geometry. These effects were assessed using the predicted flow field results from computational fluid dynamics (CFD) simulations. Prior to using the predictions, these CFD simulations were benchmarked against flow field data measured in a large scale, linear, turbine vane cascade. Good agreement occurred between the computational predictions and experimentally measured secondary flows. Analyses of the results for several different cases indicate the stagnation pressure gradient is a key parameter in determining the character of the secondary flows.

Introduction

Turbine inlet conditions in a gas turbine engine generally consist of temperature and velocity profiles that vary in the radial and pitchwise directions resulting from combustor exit conditions. Depending on the conditions, these non-uniform profiles can have a strong influence on the nature of the secondary flows in the turbine platform region, also referred to as the endwall region. Secondary flows cause aerodynamic losses, high convective heat transfer, and make it difficult to film-cool the endwall region.

The primary components of these secondary flow patterns include a leading edge horseshoe vortex and a passage vortex. The leading edge horseshoe vortex is formed as the incoming boundary layer approaches the stagnation region of the vane. This horseshoe vortex separates into pressure-side and suction-side horseshoe vortex legs. The passage vortex, having the same sense of rotation as the pressure side horseshoe vortex, develops as the flow is turned by the turbine vane or rotor blade.

The CFD simulations presented in this paper show the effects of temperature and velocity inlet profiles on these secondary flows in a linear vane cascade. The temperature and velocity profiles are considered to vary in the radial (spanwise) direction. The simulations have been done for a turbine vane geometry whereby the engine exit Reynolds number has been matched at low speed conditions. Low speed conditions were computed to allow direct comparison with measured velocities in a large-scale wind tunnel simulation. The following sections present a brief discussion of past studies, the CFD methodology and validation, the inlet profiles studied, results of the study, and a relationship with a previously given theoretical analysis.

Relevant Past Studies

An understanding of endwall secondary flows has been the subject of research in the gas turbine industry for many years. As early as 1951, Hawthorne[1] used the vorticity equation in what is commonly referred to as the Helmholtz equation to describe secondary vorticity in an inviscid, incompressible flow. This equation relates the secondary streamwise vorticity to a total pressure gradient.

In order to relate high regions of endwall heat transfer to secondary flow patterns and to provide a visual representation of flow through the turbine passage, a number of flow models have been proposed and are summarized by Sieverding[2]. In one model by Langston[3], the horseshoe vortex is split into two legs with the pressure gradient generated across the pitch of the blades transforming the pressure side leg into the passage vortex. The suction side leg exits the blade row as a counter rotating vortex inside the passage vortex. Sharma & Butler[4] showed a similar representation with the primary difference being that the suction side horseshoe vortex begins to lift off the endwall at the minimum pressure along the blade and orbit about the passage vortex. This behavior was also noted by Wang, et al.[5] In general, there are some slight disagreements in the different flow models that have been proposed but, for the most part, the models agree on the existence of the leading edge and passage vortices. Some of these disagreements may be related to the differing inlet conditions and airfoil geometries.

Two different boundary layer thicknesses of 1% and 12% of the blade span were investigated by Graziani, et al.[6] Flow visualization revealed that the saddle point associated with the vortex system moved closer to the pressure surface and further into the passage for the thinner boundary layer. There was also less crossflow associated with the thinner boundary layer.

Although there has been relatively little work published regarding secondary flow with the presence of temperature gradients, combustor exit profiles (first stage turbine stator vane inlet profiles) are far from uniform in temperature, pressure, and velocity. Some typical profiles are given in the literature by Suo[7], Halls[8], and computed by Crocker, et al.[9] The effects of inlet temperature profiles were first considered by Lakshminarayana[10] who used a steady, inviscid theoretical analysis. A generalized expression for secondary vorticity of flows having gradients of temperature, pressure or velocity was developed for compressible, inviscid flow, as will be discussed in the results section. Lakshminarayana also developed a relation for minimizing secondary flows and pointed out that in the case of a constant Mach number, resulting in a constant total pressure profile, no secondary vorticity develops. By balancing the velocity and temperature gradients normal to the endwall surface, there are no sources for generating secondary vorticity.

There is relatively little literature, both experimentally and numerically, that examines the effects of the temperature gradient typically found at the combustor exit on the secondary flows in the turbine vane passage. Although it has been theoretically shown that the temperature gradients in the absence of velocity gradients can actually reverse the rotational direction of the secondary flows in the passage, it has not been shown computationally or experimentally.

Stator Vane Geometry and CFD Approach

The airfoil geometry used for these studies was a commercial first stage stator vane, previously described by Kang, et al.[11] The vane is two-dimensional with the midspan cross-sectional geometry modeled along the entire span of the vane. The CFD simulations were computed for incompressible, viscous, low speed conditions, thereby matching the Reynolds number but not the Mach number distribution. The effect of not matching the Mach number is that the loading on the blade differs between the simulated and engine conditions. While the low-speed case has more of a fore-loaded condition, which causes stronger secondary flows, the engine case has more of an aft-loaded condition. Although these differences do occur, the basic principles illustrated by these computations are still valid. These computations allowed direct comparison with experimental data taken for the scaled-up vane experiments in the low-speed wind tunnel simulations (Kang, et al.[11]). For both the CFD analysis and wind

Nomenclature

C	true chord of stator vane
k	turbulent kinetic energy
Ma	$U_{inlet}/\sqrt{\gamma R_g T_s}$
M	mass flow through passage
n	coordinate normal to inviscid streamline
p	static pressure
P	pitch
P_o	total pressure
$P_{o,inlet}$	total pressure at inlet
$P_{o,mid}$	total pressure at the midspan
q	velocity vector
R	radius of curvature of an inviscid streamline
R_g	gas constant
Re_{ex}	Reynolds number, $C\,U_{ex}/\nu$
s	coordinate aligned with inviscid streamline
S	span of stator vane
T_s	static temperature
T_{wall}	temperature at vane endwall
T_{max}	maximum total temperature
T_{ave}	mass averaged total temperature
U_{inlet}	inlet freestream velocity
U_{ex}	exit freestream velocity
U,V,W	absolute velocity components
u,v,w	secondary flow plane transformed velocity
V_s	streamwise velocity, $u\cos\psi_{ms} + v\sin\psi_{ms}$
V_n	normal velocity, $-u\sin\psi_{ms} + v\cos\psi_{ms}$
V_z	spanwise velocity, w
X,Y,Z	absolute, stationary, coordinate system
x	distance normal to the secondary flow plane
y	distance tangent to the secondary flow plane
Y_s	pressure loss coefficient, $\dfrac{\iint \rho u \left[\dfrac{2\left(\overline{P_{o_{mix}}} - P_o\right)}{\rho U_{inlet}^2}\right] dA}{M}$
z	radial or spanwise distance
z^+	inner coordinates spanwise distance, $z\sqrt{\tau_w/\rho}/\nu$

Greek

δ	boundary layer thickness
δ_{th}	thermal boundary layer thickness
ΔP	normalized total pressure, $1 - \dfrac{(P_{0\,max} - P_0)}{(P_{0\,max} - p_\infty)}$
ε	dissipation
γ	specific heat ratio
ν	viscosity
ρ	density
Ω_S	streamwise vorticity, $\Omega_x cos(\psi_{ms}) + \Omega_y sin(\psi_{ms})$
Ω_x	x-vorticity, $\dfrac{\partial W}{\partial Y} - \dfrac{\partial V}{\partial Z}$
Ω_y	y-vorticity, $\dfrac{\partial U}{\partial Z} - \dfrac{\partial W}{\partial X}$
τ_w	wall shear stress
ψ_{ms}	midspan turning angle, $\tan^{-1}(v_{ms}/u_{ms})$

tunnel experiments, the exit Reynolds number based on chord and exit velocity was $Re_{ex} = 1.2x10^6$. The inlet and exit flow angles are 0° and 78° respectively, resulting in a smaller turning angle than many of the past studies.

The CFD simulations were completed with a commercial software package by Fluent, Inc.[12] FLUENT/UNS is a pressure-based incompressible flow solver for unstructured meshes. Second-order discretization was used for the Reynolds Averaged Navier Stokes (RANS) equations as well as the energy and turbulence equations. FLUENT/UNS is especially applicable to three-dimensional endwall flows because the unstructured mesh capabilities allow the complex geometry of the stator vane to be modeled; and because the code allows for solution-adaptive grids based on flow gradients to achieve grid-independent results.

The computational domain used for the CFD simulations is illustrated in Figure 1a while Figure 1b shows locations where the flow field predictions of the secondary flows will be compared in this paper. A symmetry boundary condition was used at the vane mid-plane while periodic conditions were assumed for the vane pitch. The inlet boundary condition was placed three-fourths of a true vane chord lengths (0.75*C*) upstream of the vane row. Two-dimensional simulations showed that the inlet boundary condition should be placed at least 0.7*C* upstream of the vane to insure the inlet is not influenced by the presence of the vane. Along the endwall at the inlet to the CFD domain, a turbulent boundary layer profile was applied as a part of the velocity boundary condition. A two-dimensional boundary layer code TEXSTAN (Crawford[13]), was used to generate the velocity, turbulent kinetic energy, and turbulent dissipation profiles for the various test cases.

An outflow boundary condition was placed one chord length downstream of the vane along a line directed with the exit angle of the vane. Again, two-dimensional CFD studies indicated that there was no influence on the solution when placing the outflow condition at one chord length downstream. An additional one-tenth of a chord was added to the periodic boundary along the direction of the blade inlet angle to avoid highly skewed cells at the outflow boundary.

Prior to performing the simulations, grid-independence was verified through a study using three different mesh sizes. For this first mesh, consisting of $4.6x10^5$ cells, the number of cells were conserved by placing the inlet and outflow boundary conditions closer to the vane (at one-half chord upstream and one-half chord downstream) with a more course node spacing at the mid-plane. Two more refined grids were used in this study, with the inlet and outlet boundary conditions described above, consisting of $8x10^5$ cells and $1.3x10^6$. As a check on the grid-independence, the average total pressure losses at several different positions through the cascade passage were calculated. Figure 2 compares the total pressure loss coefficients for all three mesh sizes as well as the other parametric cases studied. These results indicate that there are no differences between the two largest mesh sizes and an underprediction for the smallest mesh size. For these studies the $8x10^5$ cell mesh size was considered to be grid-independent.

Prior to simulating various temperature and velocity profiles, the flow field predictions along the leading edge

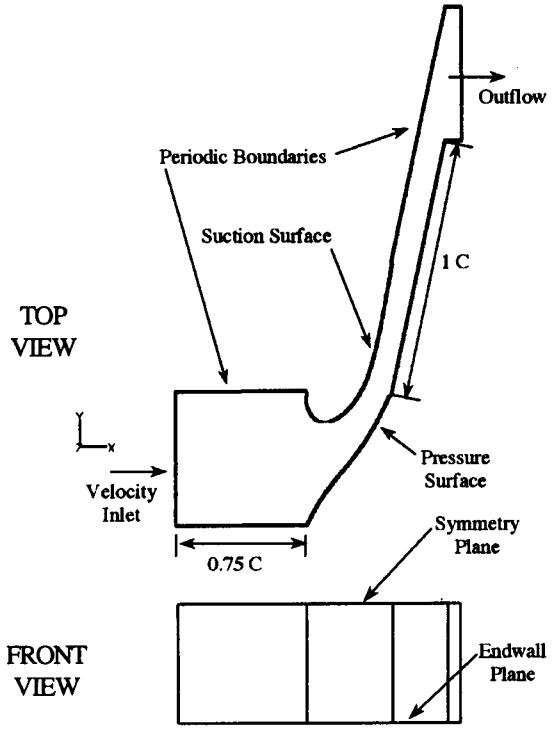

Fig. 1a Schematic of the computational domain.

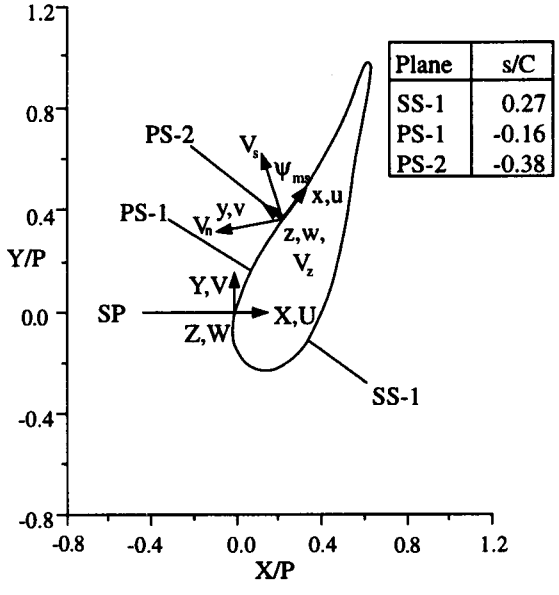

Fig. 1b Coordinates and secondary flow plane positions.

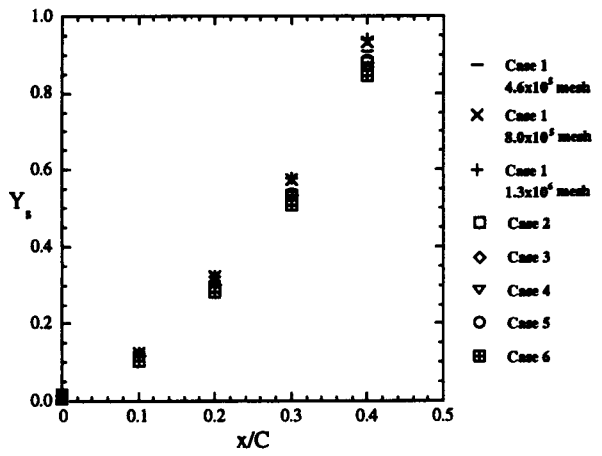

Fig. 2 Comparisons of mass averaged total presure loss.

stagnation plane were validated using laser Doppler velocimeter (LDV) measurements from a large scaled-up rig (Kang, et al.[11]). The standard k-ε (Launder and Spalding[14]) and RNG k-ε (Yakhot, et al.[15]) turbulence models were used to provide closure. Note that the node spacing near the endwall was set to achieve $30 < z^+ < 60$ in the passage to insure proper usage of the wall functions. Figures 3a - 3c present the comparison of the two turbulence model predictions with the measured flow field in the leading edge stagnation plane. The standard k-ε model predicted the location of this vortex too close to the endwall and vane stagnation while the shape of the vortex was also not captured. The RNG k-ε model most closely matched the flow pattern as well as the vorticity magnitudes. For this reason the parametric study was performed using the RNG k-ε model. The RNG k-ε model was expected to provide more accurate results since it contains additional terms in the transport equations for k and ε that are more suitable for stagnation flows and flows with high streamline curvature. The computational results of the RNG k-ε model were also compared to experimental data on two additional planes along the vane. The most notable difference seen in each of the planes is that the vortex is located slightly higher off the endwall, 1-3% of the span, in the CFD analysis than the experiments.

The primary interest of this study was to discern the horseshoe vortex legs and the passage vortex convecting through the turbine vane passage. The vectors of these vortices, which will be referred to as the secondary flow vectors, were determined by transforming the local velocities (u, v, and w in Figure 1b) into the mean flow direction (V_s, V_n, and V_z) based on that occurring at the midspan using the relations defined in the nomenclature. The secondary flow vectors are plotted using the components normal to the mean flow direction (V_n, V_z).

Parametric Study Description

Several different cases were studied to include variations in the boundary layer thickness and inlet temperature profiles with a summary given in Table 1. For all of the computed cases the static pressure is constant at the inlet, and the static temperature is specified. The first case shown in Table 1 illustrates what will be referred to as the baseline case. This case was computed to compare with experimental data that had a constant inlet static temperature profile and a turbulent boundary layer that was 9.1% of the full vane span. Results from the baseline boundary layer thickness, a thin boundary layer (1.8% span), and four cases with various radial temperature gradients will be compared in this paper.

The total temperature profiles used in Cases 4, 5, and 6 are similar to that used by Boyle and Giel[16]. This profile

Table 1. Summary of Baseline and CFD Test Matrix

Case Number	Velocity Profile Characterisitics	T_{wall}/T_{max}	T_{wall}/T_{avg}
1 (Baseline)	$\delta/S = 9.1\%$	1	1
2	$\delta/S = 1.8\%$	1	1
3	$\delta/S = 9.1\%$	0.89	0.92
4	$\delta/S = 9.1\%$	0.63	0.73
5	U = Constant	0.63	0.73
6	Ma = Constant	0.63	0.73

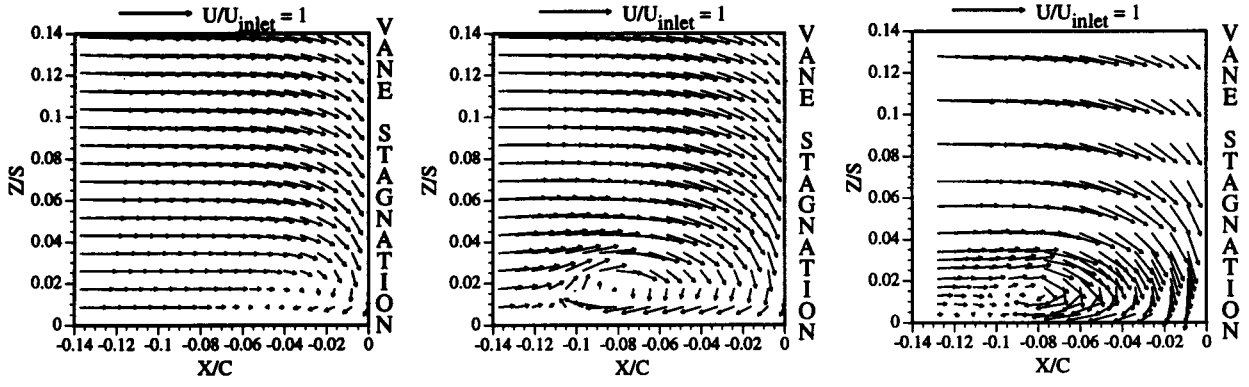

a) k-ε turbulence model b) k-ε RNG turbulence model c) Experimental LDV measurements

Fig.3 a-c Comparison of turbulence models and experimental LDV measurements at the leading edge stagnation plane.

has a maximum to minimum total temperature ratio (T_{max}/T_{wall}) of 1.6, which is still less than measurable factors up to 2.0 in an actual gas turbine (Butler et al[17]). The normalized inlet temperature profiles used for these simulations are shown in Figure 4. For the constant Mach number case the mass averaged static temperature is equal to the uniform temperature of the baseline. Since the Mach number is low, there are only slight variations of total temperature between Cases 4, 5, and 6 due to the differences in velocity profiles. The normalized velocity profiles used for these cases are shown in Figure 5. For the cases of the constant velocity and constant inlet Mach number (Cases 5 and 6) there is only a thin boundary layer that forms as the flow approaches the vanes.

Flow Field Results

The CFD results were analyzed by flow visualization with particle pathlines, secondary flow velocities, normalized total pressure contours (ΔP, see nomenclature), and normalized streamwise vorticity ($\Omega_S C/U_{in}$) contours in the planes illustrated in Figure 1b for the cases described in Table 1. Note that the coordinate system is such that $y/P = 0$ is always located at the vane surface and the observation direction is looking downstream for planes on both the suction and pressure surfaces. First, the effect of different boundary layer thicknesses will be addressed followed by a discussion on the effect of different temperature profiles, and finally a comparison with the theoretical analyses is presented.

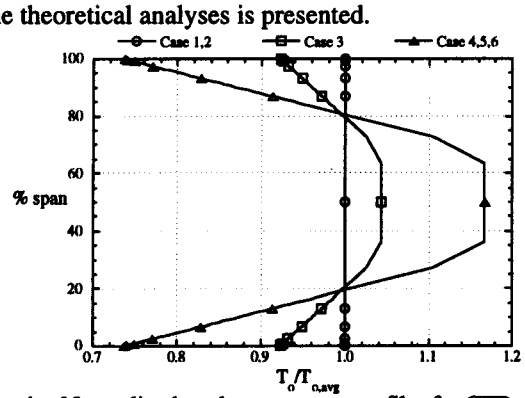

Fig. 4 Normalized total temperature profiles for CFD cases.

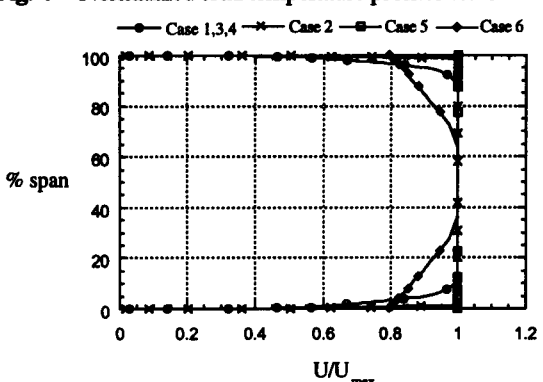

Fig. 5 Normalized velocity profiles for CFD cases.

Effect of Inlet Boundary Layer Thickness

Tracing the pathlines of particles at strategically placed locations upstream of the vanes showed flow patterns through the passage for the baseline case that are similar to those described earlier. Figure 6 shows pathlines for the baseline case released from a region that includes 0 - 13% of the span at X/C = -0.17. The shading of the pathlines indicate the magnitude and direction of the spanwise velocity component (V_z). As the pathlines approach the vane stagnation, a horseshoe vortex forms and splits into a suction side and pressure side leg. Pathlines released above the boundary layer (9.1% span) are pulled down toward the endwall with the strongest spanwise velocities occurring on the suction side. The pathlines along the suction surface are swept into the suction side horseshoe vortex, while the pathlines along the pressure side move across the passage at the endwall. The flow visualization shows how areas of high heat transfer are produced as the horseshoe or passage vortex brings hot mainstream gas onto the endwall region. The strong spanwise velocity component at the leading edge is in agreement with a high Stanton number region in the endwall heat transfer experiments of Graziani, et al.[6] and

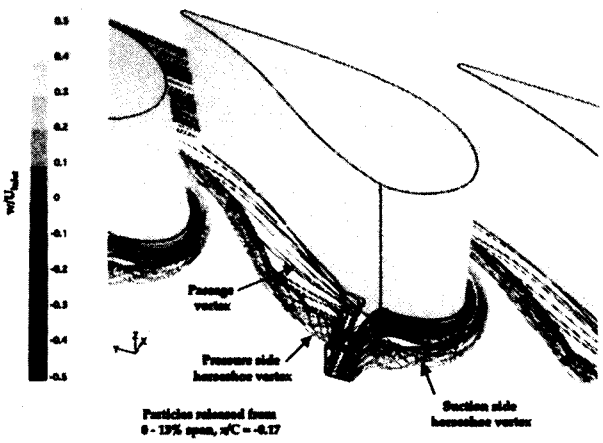

Fig. 6 Particle pathlines for Case 1, $\delta S = 0.091$.

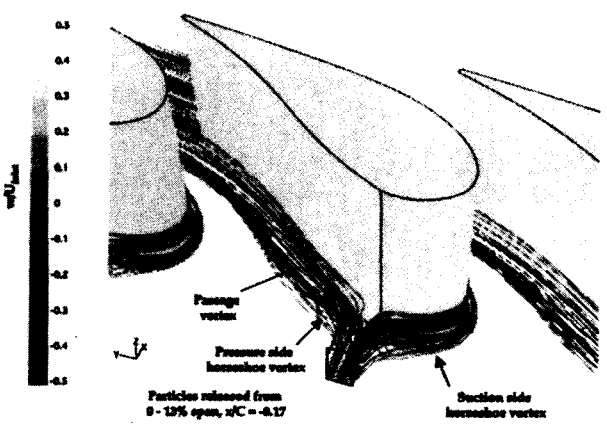

Fig. 7 Particle pathlines for Case 2, $\delta S = 0.018$.

Kang, et al.[7] In agreement with Ho and Lakshminarayana[18], Gregory-Smith, et al.[19], and Kang [20] is that the suction side horseshoe vortex begins to diffuse and dissipate as it is encountered by the passage vortex beyond Plane SS-1.

Pathlines for the thinner boundary layer (Case 2) in Figure 7 show a flow pattern similar to the baseline case in the development of the horseshoe and passage vorticies. One of the differences between these two cases is that the leading edge horseshoe vortex forms much closer to the leading edge of the vane for the thinner boundary layer. Pathlines just outside of the boundary layer also flow down the vane surface, while pathlines further from the endwall flow along the curvature of the blade as those pathlines are now in the inviscid region. For the thinner boundary layer, the vortices show a smaller magnitude in spanwise velocity and a smaller region of the endwall being affected by the secondary flows. Once again this is in agreement with the results of Graziani, et al.[6] where they compared different inlet boundary layer thicknesses on endwall heat transfer measurements.

Secondary flow patterns and streamwise vorticity contours on plane PS-2 are illustrated in Figures 8a and 8b for Cases 1 and 2. This plane shows the passage vortex,

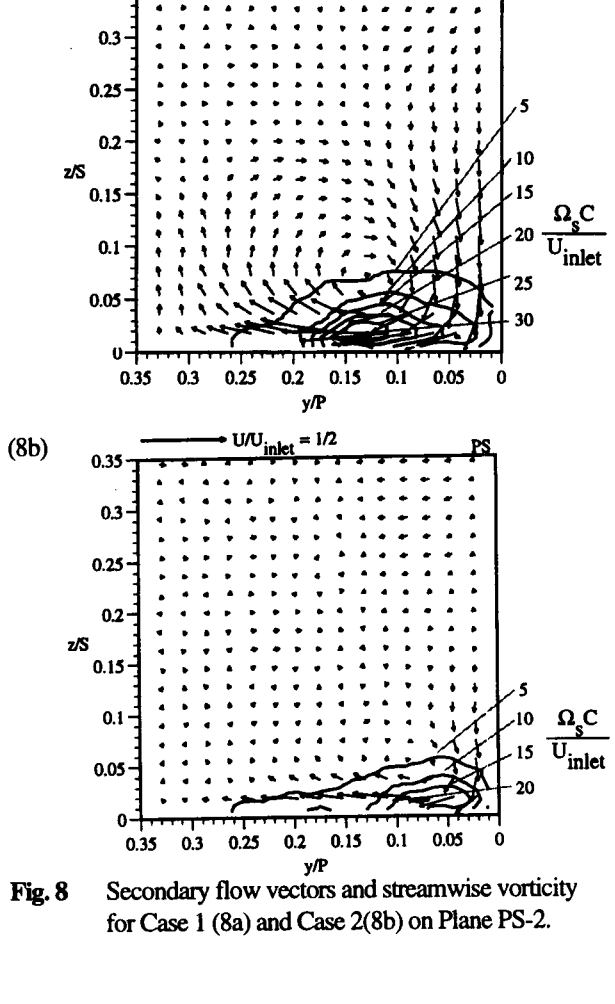

Fig. 8 Secondary flow vectors and streamwise vorticity for Case 1 (8a) and Case 2(8b) on Plane PS-2.

which is still close to the pressure surface at this location, and the relative magnitudes of secondary streamwise vorticity for each case. From the velocity vectors it is evident that the passage vortex occupies a much larger region of the endwall for the thicker boundary layer and the core is further removed from the pressure surface. Similar to the results reported by Gregory-Smith, et al.[19], the streamwise vorticity contours peak near the endwall surface. The primary difference between Cases 1 and 2 is that the thicker boundary layer (Case 1) has significantly larger contour levels than the thinner boundary layer case (Case 2). Another difference is that the peak level for the thinner boundary layer occurs closer to the vane than the thicker boundary layer case.

Effect of Spanwise Temperature Profiles

Each of the cases with a non-uniform inlet temperature, Cases 3 through 6, had a thermal boundary layer thickness that was 32% of the vane span and varied linearly from the wall temperature to the freestream temperature (as seen in Figure 4). Results from each of these cases were evaluated to determine the effect of temperature gradients on secondary flow. Plots of total pressure at the leading edge stagnation plane as well as the secondary velocity vectors superimposed with streamwise vorticity contours for Plane SS-1 are given for several cases in Figures 9a-b, Fig 10a-b, Fig. 11a-b, and Fig. 12a-b.

Figure 9b presents the secondary flow vectors and streamwise vorticity for the baseline case in a plane normal to the suction surface, SS-1. This plot illustrates that while the suction side horseshoe vortex occupies only 12% of the span, the passage vortex from the neighboring vane extends as high as 25% of the span. To show the effect of the smaller temperature gradient, the secondary flow patterns and streamwise vorticity results from Case 3, given in Figure 10b, varied only slightly from the baseline case (Figure 9a). The spanwise component of velocity along the vane surface was reduced outside the boundary layer, but the overall secondary flow pattern did not change.

When a larger temperature gradient was applied, as in Case 4, the flow patterns showed a significant difference from the baseline case as seen when comparing Figures 9b and 11b. For Case 4, the secondary flow pattern indicates that the center of the passage vortex moved closer to the pressure side/endwall corner. The temperature gradient caused the flow to actually split with flow turning toward the endwall region in the bottom 14% of the span and flow turning toward the mid-span above the 14% span location. The flow turning toward the endwall formed the passage vortex while the flow turning toward the mid-span formed a weaker counter-rotating vortex that extended to the midspan.

The flow pattern was completely changed in Case 5, illustrated in Figure 12b, with the combination of a con-

stant velocity profile and large temperature gradient. Here, the flow at the leading edge and throughout the passage moved up the pressure side vane surface from endwall to midspan rather than impinging on the endwall surface as was seen by the pathlines in Figure 5 and Figure 6. The magnitude of these reversed secondary flows are slightly less than that of the baseline case and the streamwise vorticity is smaller and concentrated near the endwall but, never-the-less the flow pattern has significantly changed. The existence of these strong profiles shows the large effect which the combustor exit profile can have on turbine vane secondary flows and endwall heat transfer.

With a constant Mach number inlet condition, Case 6, no horseshoe or passage vortices were formed. While there is still a slight cross-pitch velocity due to the pressure gradient, the pathlines in Figure 13 most distinctly show that the flow is not pulled onto the endwall for the constant inlet Mach number. Any vorticity present at the leading edge, is due only to the thin boundary layer that develops along the endwall.

Theoretical Analysis

Since the combustor exit plane has very large spanwise and pitchwise gradients in velocity and temperature it is important to understand how to predict what combinations of the two parameters minimize secondary flows. Through this parametric study and in agreement with the theoretical analysis by Lakshminarayana[11], it has been concluded that the driving factor is the total pressure profile at the leading edge stagnation plane. The computed results show that the streamwise component of vorticity through the passage scales with the gradient of the total pressure. For the stagnation plane at the leading edge of the turbine vane, a simplified description of the developing streamwise vorticity can be given using the absolute components *XYZ*, *UVW*, $\Omega_x\Omega_r\Omega_z$. The Helmholtz equation (equation of motion for rotational flow) for incompressible flow using the absolute components of vorticity can be written as:

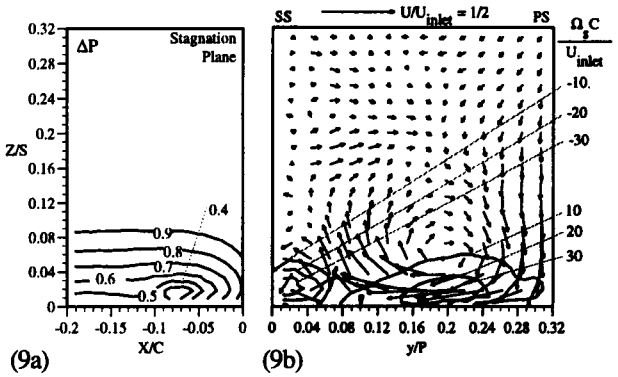

Fig. 9 Pressure contours at stagnation (9a), and secondary vectors and streamwise vorticity (9b) on SS-1 for Case 1.

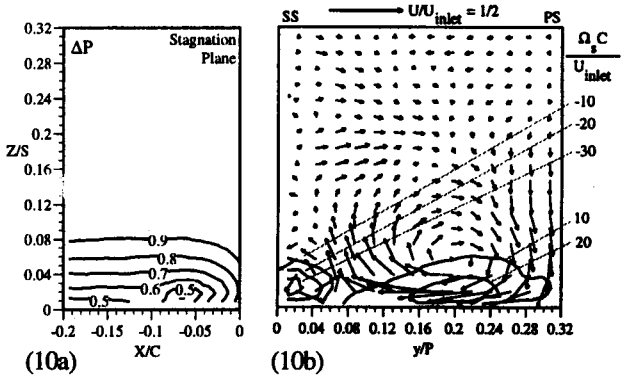

Fig. 10 Pressure contours at stagnation (10a) and secondary vectors with streamwise vorticity (10b) on SS-1 for Case 3.

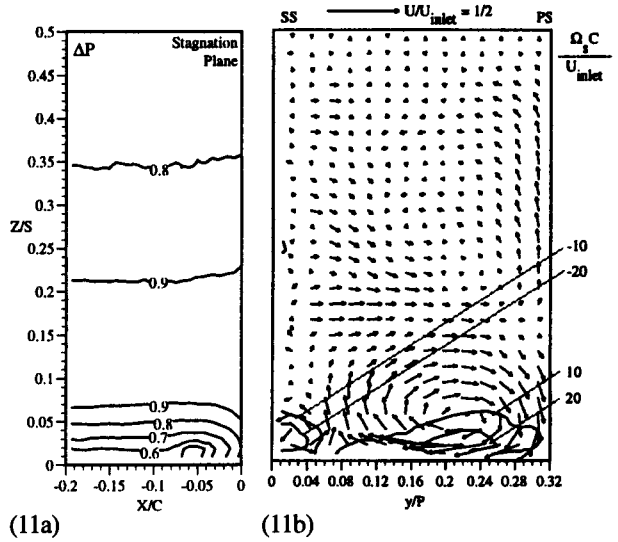

Fig. 11 Pressure contours at stagnation (11a) and secondary vectors with streamwise vorticity (11b) on SS-1 for Case 4.

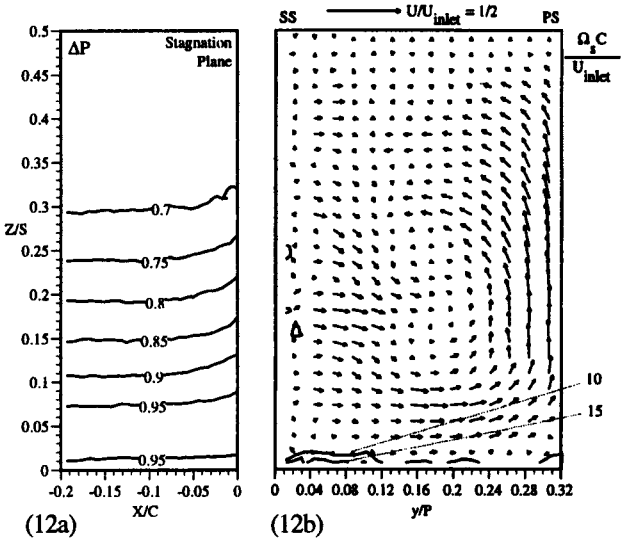

Fig. 12 Pressure contours at stagnation (12a) and secondary vectors with streamwise vorticity (12b) on SS-1 for Case 5.

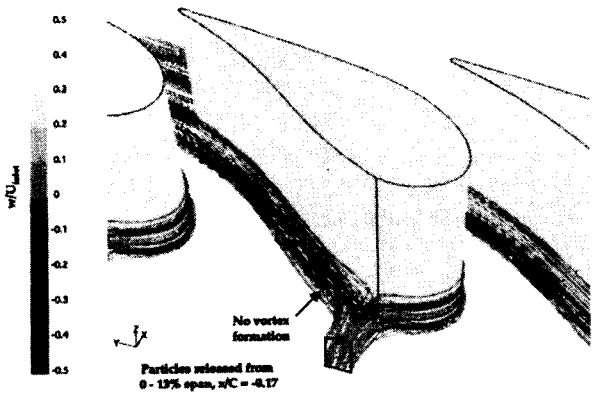

Fig. 13 Pathlines for constant inlet Mach number, Case 6.

$$q \times \Omega = \frac{1}{\rho} \nabla p_0 \tag{1}$$

By taking the spanwise component of this equation the relationship between inlet vorticity components and spanwise total pressure gradients is given. Spanwise total pressure gradients are of concern in this paper.

$$u\Omega_Y - v\Omega_X = \frac{1}{\rho} \frac{\partial p_0}{\partial Z} \tag{2}$$

These equations can be simplified to obtain a prediction of streamwise vorticity at the leading edge based on several assumptions. For the cases analyzed with a temperature gradient use of the incompressible equation of motion can be justified because the Mach number is low. At the inlet and the upstream portion of the leading edge stagnation plane, Plane SP, the flow is completely aligned with the X direction, thus the gradients associated with the V and W components of velocity are small relative to the boundary layer or temperature spanwise gradients. Using the equation given in the nomenclature at the leading edge, the streamwise vorticity is determined from the midspan flow angle measured with respect to the leading edge stagnation plane. This results in the following prediction for streamwise vorticity at the leading edge:

$$\Omega_s = \frac{1}{U\rho} \frac{\partial p_o}{\partial Z} \sin \psi_{ms} \tag{3}$$

Since the streamlines are curved at the vane stagnation (up to ~25°), and there is a large component of Ω_Y due to total pressure gradients in the incoming boundary layer (at least for the baseline case), then streamwise vorticity will develop at the leading edge in the form of the horseshoe vortex. Although the streamwise vorticity is small in this region because the turning angle is small, each of the cases analyzed shows that the measure of streamwise vorticity at the leading edge dictates the level of secondary flows throughout the passage. The passage vortex also forms as the turning angle increases on the pressure surface. The normal component of vorticity (Ω_Y at the leading edge plane and Ω_n throughout) is assumed constant in inviscid flow theory. True viscous effects tend to dissipate and diffuse the vorticity component somewhat. As the turning of the flow becomes significant, however, the streamwise vorticity also increases. This effect is apparent in the suction side leg of the horseshoe vortex (Figure 6). The large spanwise velocity components on the leading edge suction surface can be attributed to the large turning of the streamlines in this region. Similarly the vorticity tends to decrease further back along the suction surface where the suction side horseshoe vortex dissipates due to both the viscous actions decreasing the normal component of vorticity and the reduced turning.

Beyond the leading edge, as the three-dimensional flow develops, similar arguments can be made using an intrinsic coordinate system as discussed by Lakshminarayana[11]. For the constant Mach number case, which gives a constant total pressure along the span since the static pressure is constant, the results indicated that no vortex structure formed at the leading edge or within the passage. Only small levels of streamwise vorticity were present in the passage as a shear layer forms on the endwall. This streamwise vorticity is distinctly different than a vortex structure. This is not to say that with no leading edge vortex there can be no passage vortex but rather to say that with no leading edge vortex, a passage vortex would still form independently if a spanwise total pressure gradient was present in the passage. For the constant Mach number case, there were no total pressure gradients to form either the leading edge or the passage vortices. This concept was introduced in early work by Hawthorne[1] stating "secondary circulation remains unchanged if streamlines are geodesics on surfaces of constant total pressure."

Normalized total pressure contours at the leading edge, Plane SP (Figures 9a,10a,11a, and 12a) graphically display the relationship between stagnation pressure gradients and secondary flows further in the passage, Plane SS-1 (Figures 9b, 10b, 11b, and 12b). The presence of total pressure gradients approaching the leading edge drive flow in the direction of decreasing pressure. This results in the formation of the horseshoe/passage vortex for all of the cases presented except for Case 5 in which the gradients caused a reversed, large vortex extending from the endwall to midspan. In the case of a constant inlet Mach number (Case 6), the total pressure is uniform resulting in no secondary flows, as was shown in Figure 13.

In comparing Cases 3 and 4 it is clear that the secondary flows near the endwall (Figures 10a-b, 11a-b) show only a slight difference between these cases and the baseline case even though there is a variation in the total temperature profiles. The real difference that occurs be-

tween these cases is further away from the endwall and towards the midspan where the flow actually forms another vortex as shown in Figure 11b. This effect directly corresponds to the total pressure contours, but cannot be detected in the streamwise vorticity.

Conclusions

These results indicate the importance of knowing the exiting combustor conditions in order to predict the secondary flows that occur in the endwall region of a stator vane. Prior to using CFD to simulate the effects of different velocity and temperature profiles, a benchmark was done between the secondary flow predictions and those measured in a low-speed wind tunnel simulation. Good agreement was found between the predictions and measurements.

The flow field results indicated the importance that the stagnation pressure gradients at the inlet to the turbine vane cascade have on the secondary flows. In fact, the flow field results indicated that when a strong enough temperature gradient occurs such that the stagnation pressure gradient is altered it is possible to have counter-rotating vortices in the passage. One of these counter-rotating vortices is the passage vortex while the other vortex drives the flow away from the endwall toward the midspan. These results also showed that when no stagnation pressure gradient was present, as simulated by a constant Mach number with a constant static pressure, no leading edge or passage vortex developed in the turbine vane passage. The results presented in this paper are in agreement with previously reported theoretical analyses.

Acknowledgments

The authors gratefully acknowledge Bill Kvasnak and Fred Soechting at United Technologies-Pratt & Whitney for their support on this project.

References

1. Hawthorne, W. R., "Secondary Circulation in Fluid Flow," *Proc. Roy. Soc. A*, Vol. 206, 1951, p.374.
2. Sieverding C. H., "Recent Progress in the Understanding of Basic Aspects of Secondary Flows in Turbine Blade Passages," *J of Engineering for Gas Turbines and Power*, Vol. 107, 1985, p. 248.
3. Langston, L. S., "Crossflows in a Turbine Cascade Passage," *J of Engineering for Power*, Vol. 102, 1980, p. 866.
4. Sharma, O. P. and Butler, T. L., "Predictions of Endwall Losses and Secondary Flows in Axial Flow Turbine Cascades," *J of Turbomachinery*, Vol. 109, 1987, p. 229.
5. Wang, H. P., Olson, S. J., Goldstein, R. J. and Eckert, E. R. G., "Flow Visualization in a Linear Turbine Cascade of High Performance Turbine Blades," *J of Turbomachinery*, Vol. 119, 1997, p. 1.
6. Graziani, R. A., Blair, M. F., Taylor, J. R. and Mayle, R. E., "An Experimental Study of Endwall and Airfoil Surface Heat Transfer in a Large Scale Turbine Blade Cascade," *J of Engineering for Power*, Vol. 102, 1980, p. 257.
7. Suo M., "Turbine Cooling" in *Aerothermodynamics of Aircraft Engine Components*, G.C. Oates editor, AIAA, Inc. publisher., 1985
8. Halls, B. A., "Nozzle Guide Vane Cooling," AGARD, CP No. 73, Paper 25, 1970.
9. Crocker, S. C., Nickolaus, D., and Smith, C. E., "CFD Modeling of a Gas Turbine Combustor from Compressor Exit to Turbine Inlet", ASME Paper 98-GT-184.
10. Lakshminarayana, B., "Effects of Inlet Temperature Gradients on Turbomachinery Performance," *ASME J of Engineering for Power*, Vol. 97, 1975, p. 64.
11. Kang, M. Kohli, A., and Thole, K.A., "Heat Transfer and Flowfield Measurements in the Leading Edge Region of a Stator Vane Endwall," ASME Paper 98-GT-173.
12. Fluent Inc., Fluent User's Guide, Version 4.2., 1996 (Fluent Inc.: New Hampshire)
13. Crawford, M.E., "Simulation Codes for Calculation of Heat Transfer to Convectively-Cooled Turbine Blades," 130 pp., a set of 4 lectures in Convective Heat Transfer and Film Cooling in Turbomachinery, T. Arts, ed., Lecture Series 1986-06, von Karman Institute for Fluid Dynamics, Rhode-Saint-Genese, Belgium.
14. Launder, B.E. and Spalding D.B., "The Numerical Computation of Turbulent Flows," Computer Methods in Applied Mechanics and Engineering, 3:269-289, 1974.
15. Yakhot V., Orszag S., Thangman, S., Gatski, T.B., and Speziale, CG., "Development of Turbulence Models for Shear Flows by a Double Expansion Technique," *Phys. Fluids* A 4 (7), 1992, p. 1510.
16. Boyle, R.J. and Giel, P.W., "Prediction of Nonuniform Inlet Temperature Effects on Vane and Rotor Heat Transfer," ASME Paper 97-GT-133.
17. Butler, T. L., Sharma, O.P., Joslyn, H.D., Dring, R.P., "Redistribution of an Inlet Temperature Distortion in an Axial Flow Turbine Stage," *AIAA J of Propulsion and Power*, Vol. 5, No.1, 1989, p. 64.
18. Ho, Y. and Lakshminarayana, B., "Computational Modeling of Three-Dimensional Endwall Flow Through a Turbine Rotor Cascade with Strong Secondary Flows," *J of Turbomachinery*, Vol. 118, 1996, p. 250.
19. Gregory-Smith, D. G., Graves, C.P., and Walsh, J. A., "Growth of Secondary Losses and Vorticity in an Axial Turbine Cascade," *J of Turbomachinery*, Vol. 110, 1988.
20. Kang, M. and Thole, K. A., "Detailed Measurements in the Endwall Region of a Gas Turbine Stator Vane," CHTL Report 98-3, August 1998.